metals

Article

3D Printing of Mg-Based Bulk Metallic Glasses with Proper Laser Power and Scanning Speed

Zijian Zhao [1], Guang Yang [1,*] and Kun Zhao [2,*]

[1] School of Mechanical Engineering, Hebei University of Science and Technology, 26 Yuxiang Road, Shijiazhuang 050018, China
[2] School of Sciences, Hebei University of Science and Technology, 26 Yuxiang Road, Shijiazhuang 050018, China
* Correspondence: y_guang@126.com (G.Y.); zhk3415@163.com (K.Z.)

Abstract: Additive manufacturing allows for the fabrication of large-sized metallic glasses with complex geometries, which overcomes the size limitation due to limited glass-forming ability. To investigate the effect of synthesis parameters on the Mg-based metallic glasses, $Mg_{65}Cu_{20}Zn_5Y_{10}$ was fabricated by laser-based powder bed fusion under different scanning speeds and laser powers. For high energy density, the samples showed severe crystallization and macrocracks, while for low energy density, the samples contained pore defects and unfused powders. Three-dimensionally printed samples were used for the compression test, and the mechanical properties were analyzed by Weibull statistics. Our work identifies proper parameters for 3D printing Mg-based metallic glasses, which provide a necessary, fundamental basis for the fabrication of 3D-printed Mg-based metallic glass materials with improved performance.

Keywords: additive manufacture; selective laser melting; Mg-based bulk metallic glasses; microstructure; mechanical performance

check for updates

Citation: Zhao, Z.; Yang, G.; Zhao, K. 3D Printing of Mg-Based Bulk Metallic Glasses with Proper Laser Power and Scanning Speed. *Metals* **2022**, *12*, 1318. https://doi.org/10.3390/met12081318

Academic Editors: Jamieson Brechtl, Peter K. Liaw and Andrea Di Schino

Received: 22 June 2022
Accepted: 2 August 2022
Published: 5 August 2022

1. Introduction

Bulk metallic glasses(BMGs) are metallic materials absent of long-range order in the arrangement of atoms. Compared to traditional crystalline metals, BMGs show unique properties, such as high strength, high elastic limit, high corrosion resistance and high wear resistance [1–4]. The formation of BMGs needs a high cooling rate. A fast cooling rate requires a large surface-to-volume ratio, so the geometric size and shape of BMG samples prepared by the traditional rapid casting method are greatly limited. The development of a novel BMG-forming process has always been one of the hot topics. Three-dimensional printing is a rapidly developing research field, and it has been applied in various industries [5–7]. Laser-based powder bed fusion (LB-PBF), also known as selective laser melting (SLM), uses a high-energy laser to selectively melt metallic powder particles and to fuse them locally with the layer underneath. The repetitive process allows components to be built layer by layer. The cooling rate in LB-PBF process can be as high as 10^4–10^7 K/s, which satisfies the cooling rate for most BMG systems [8]. As LB-PBF overcomes the limitation of geometric size and shape in BMGs, a rising number of studies have been focused on preparing BMGs by 3D printing in different systems, such as Zr-, Fe-, Ti-, and CuZr-based metallic glasses [9–12]. For recent and comprehensive reviews of 3D printing metallic glasses, see ref [8,13] Mg-based BMGs are promising candidates for engineering materials, such as those used in the automobile and aircraft industries, because of their marvelous properties, such as light density, high strength, and being low cost and environmentally friendly. Mg-based BMGs can improve corrosion behavior significantly and show great potential for development in a new generation of biodegradable implants [14–16]. However, the additive manufacture of Mg-based BMGs does not currently exist. $Mg_{65}Cu_{20}Zn_5Y_{10}$(at.%) BMG has good glass-forming ability, and it is a prototype of Mg-based metallic glass composites with a high specific strength, which is also suitable for 3D printing [17,18]. In this study, we report the fabrication of $Mg_{65}Cu_{20}Zn_5Y_{10}$ metallic glasses by LB-PBF. The effect of scanning speed and laser power on the microstructure evolution of the samples is discussed. The 3D-printed samples show scattered fracture strength, and the mechanical performance is analyzed by Weibull statistics. The information will provide the necessary, fundamental basis for the fabrication of 3D-printed Mg-based BMG materials with improved performance.

2. Materials and Methods

The powders with nominal composition $Mg_{65}Cu_{20}Zn_5Y_{10}$(at.%) were produced by inert gas atomization. As shown in Figure 1a, the powders have an approximately spherical shape in the SEM image. The size distribution of the powder was measured by laser particle size analyzer (HELOS (H3751)and RODOS/T4, R4, SYMPATEC GmbH, Clausthal-Zellerfeld, Germany), and the result is shown in Figure 1b. The LB-PBF experiment was performed by commercial machine Renishaw AM250 (Renishaw, Wotton-under-Edge, UK). The forming chamber was vacuumed and protected by argon gas with oxygen content below 250 ppm. The layer thickness was 50 μm. Unidirectional scanning vectors were used and rotated by 67° in adjacent layers. The hatch spacing between scanning lines was 60 μm. The power of the laser was from 80 to 110 W, and the scanning speed was from 900 to 1200 mm/s. See Table 1 for details of laser power and scanning speed. Specimens with dimensions of 10 mm × 5 mm × 6 mm were fabricated by SLM for microstructure test, and samples of 2 mm × 2 mm × 4 mm were fabricated for compression test. The microstructure of the samples was analyzed by X-ray diffraction (XRD, D8-ADVANCE, Bruker, Munich, Germany) with Cu K_α target, scanning angle from 20° to 80°, scanning speed of 4° per minute, and scanning step of 0.02. The crystallinity was obtained by calculating the ratio of the area under the sharp peaks compared to that of the broad peak using XRD data. The cross-section of the sample was analyzed by scanning electron microscopy (SEM, JSM-IT500LA, JEOL Ltd., Tokyo, Japan) with BSE detector. Then, 2 mm × 2 mm × 4 mm cuboid samples were used for quasi-static uniaxial compression test, and they were measured with a strain rate of 1×10^{-4} s^{-1} using a universal mechanical test machine (UTM6503, Shenzhen Suns Technology stock Co. Ltd. Shenzhen, China) at room temperature. The Vickers hardness (Hv) was determined by microhardness tester (QnessGmbH Q30, ATM Qness GmbH, Mammelzen, Germany) with a load of 1 Kg at room temperature.

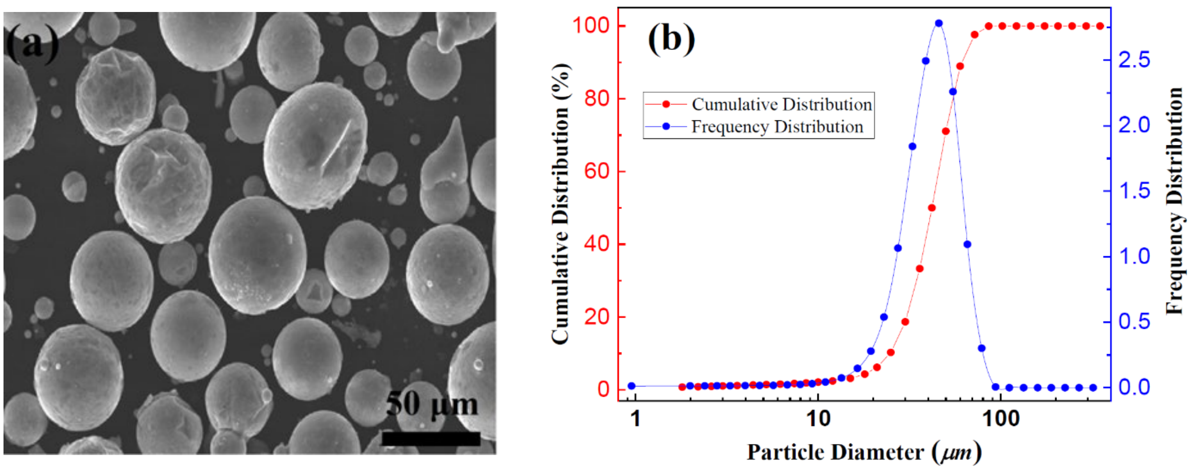

Figure 1. Mg-based alloy powders: (**a**) SEM image of the powders. (**b**) Size distribution of the powders.

3. Results

$Mg_{65}Cu_{20}Zn_5Y_{10}$ metallic glasses can be fabricated by LB-PBF in a narrow parameter window. Figure 2a shows the photo image of samples in good condition. These samples were fabricated for a laser scanning speed of 1000 mm/s and laser power of 100 W. If the scanning speed is 900 mm/s and the laser power is 110 W, the samples usually have macrocracks. As shown in Figure 2b, the cracks are roughly parallel to the layers. While the scanning speed is 1200 mm/s and the laser power is 80 W, unfused powder appears inside the samples and the samples do not show metallurgical combination, as shown in Figure 2c.

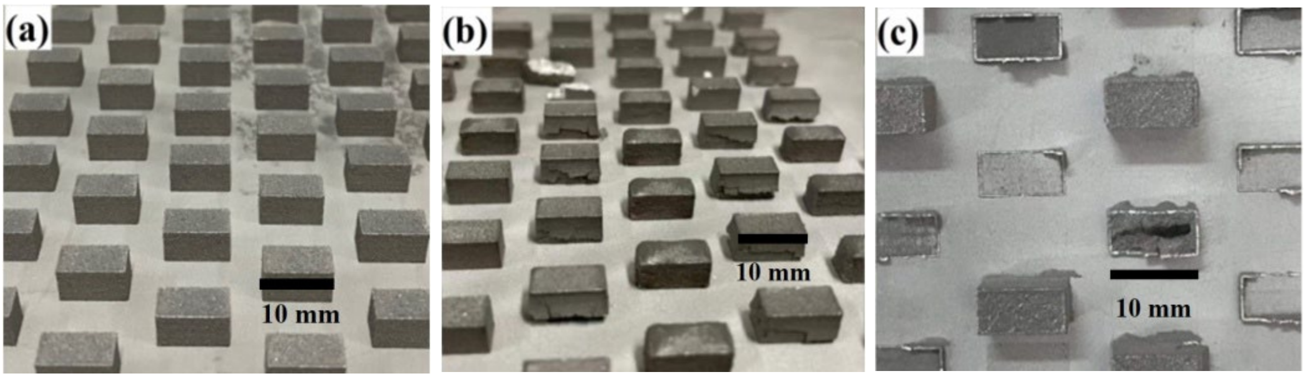

Figure 2. Photo image of 3D-printed Mg-based metallic glasses: (**a**) Samples in good condition (scanning speed: 1000 mm/s, and laser power: 100 W). (**b**) Samples with macrocracks (scanning speed: 900 mm/s, and laser power: 110 W). (**c**) Samples with unfused powders (scanning speed: 1200 mm/s, and laser power: 80 W).

3.1. Effect of Scanning Speed on the Microstructures

The influence of laser power combined with scanning speed on the microstructure of the samples was investigated. Figure 3a shows the XRD patterns of the 3D-printed Mg-based metallic glasses with fixed laser power of 100 W. When the scanning speed is 900 mm/s, the samples show sharp crystalline peaks in an XRD curve. These sharp peaks are marked with symbols, such as a red solid circle, a blue diamond and a black circle, to indicate the crystalline phase. The main crystalline phase is Mg_2Cu, and there are also some Y_2O_3 and unknown phases. These crystalline phases are consistent with the cast $Mg_{65}Cu_{20}Zn_5Y_{10}$ of low cooling rate [17]. Analysis from the XRD curve shows that the crystallinity of the sample is 31% under such processing parameters. When the scanning speed increases to 1000 mm/s, only tiny crystalline peaks are on the broad peak. The crystallinity decreases to 23% under such processing parameters. When the scanning speed increases to 1100 mm/s, the XRD patterns do not show an obvious change, indicating a similar microstructure of the sample. When the scanning speed increased to 1200 mm/s, the XRD shows sharp crystalline peaks again, with a crystallinity of 32%. Figure 3b shows an SEM image of the sample fabricated at a scanning speed of 900 mm/s. The sample shows an alternative configuration of melting pools (MPs) and heat-affected zones (HAZ). Typically, MPs are comprised of a monolithic glass, whereas the HAZs often partially crystallize [19]. Figure 3c shows the SEM of the sample fabricated at a scanning speed of 1000 mm/s. The sample still shows an alternative configuration of MPs and HAZs. However, the MPs become wider and the HAZs become thinner, indicating a more amorphous phase inside the samples. It has been reported that increments of scanning speed would inhibit the crystallization process [9]. As the scanning speed increases to 1000 mm/s, the SEM image shows that there are less crystalline phases in the HAZs. As the scanning speed increases to 1200 mm/s, a large number of pore defects appear inside the samples, as shown in Figure 3d.

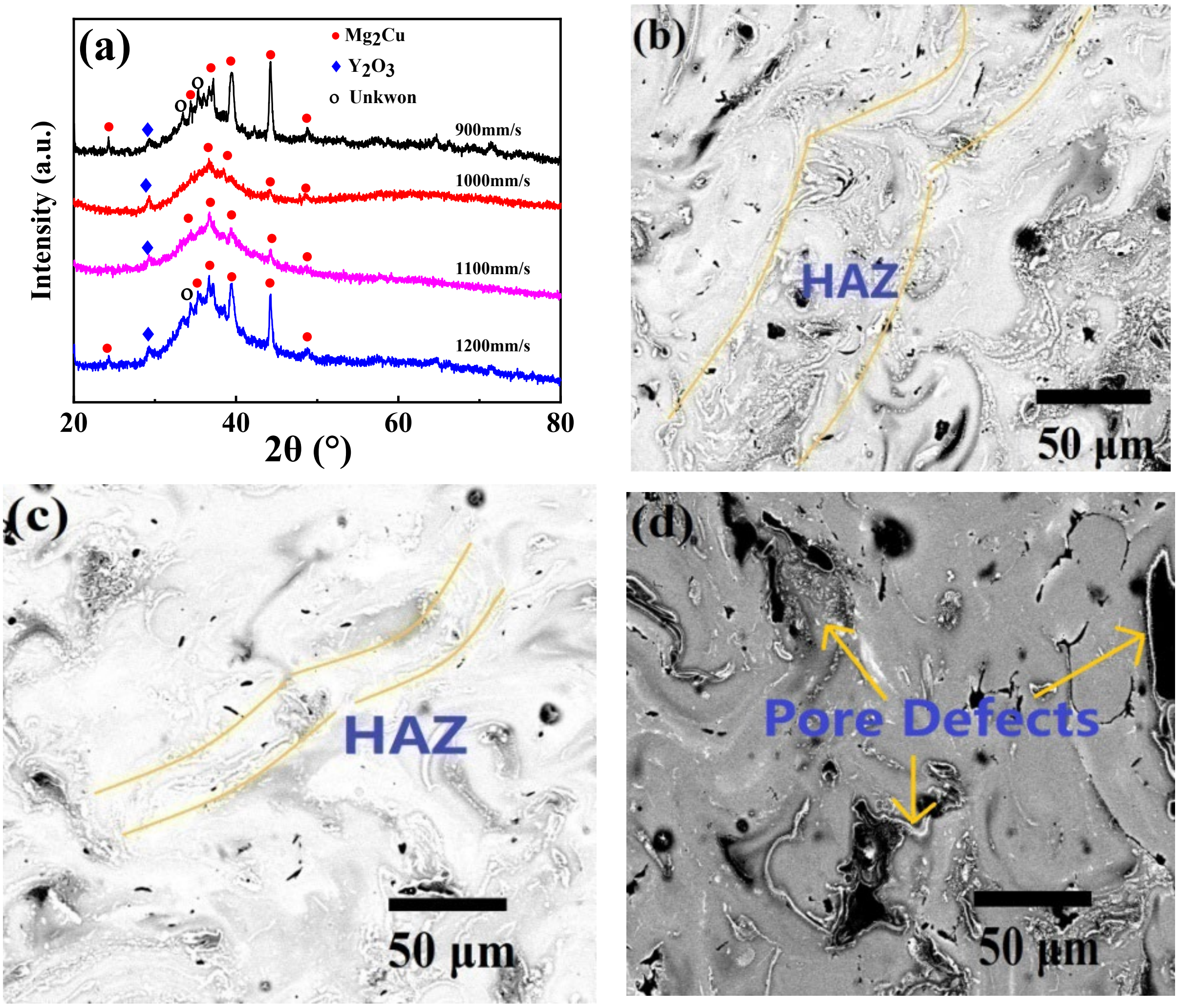

Figure 3. XRD and SEM of 3D-printed Mg-based metallic glasses with laser power of 100 W: (**a**) XRD of the samples with different scanning speed. (**b**) SEM of the cross-section at scanning speed of 900 mm/s. (**c**) SEM of the cross-section at scanning speed of 1000 mm/s. (**d**) SEM of the cross-section at scanning speed of 1200 mm/s.

3.2. Effect of Laser Power on the Microstructures

The laser power also has an influence on the microstructures. Figure 4 shows the XRD and SEM results of 3D-printed Mg-based metallic glasses at a scanning speed of 1000 mm/s. Figure 4a shows the XRD patterns of 3D-printed samples fabricated at different laser powers. When the laser power is as high as 110 W, sharp crystalline peaks appear on the XRD curves. The peaks in the XRD curve indicate that the crystalline phases are mainly Mg_2Cu with some Y_2O_3 and unknown phase. The crystallinity is 29% under such processing parameters. When the laser power is 100 W, the XRD curve shows a minor crystalline peak, indicating that the crystalline phase is inhibited as the laser power decreases. However, an obvious crystalline peak reappears when the laser power deceases to 90 W and 80 W, with a crystallinity of 28% and 30%, respectively. Figure 4b shows the SEM image of the sample fabricated at a laser power of 110 W. Severe crystallization can be found in the HAZs. When the laser power decreases to 100 W, there are less crystalline phases in the HAZs, which have already been shown in Figure 3c. When the laser power decreases to 80 W, pore defects appear on the SEM image. As shown in Figure 4c, the irregular pore defects are several tens of microns.

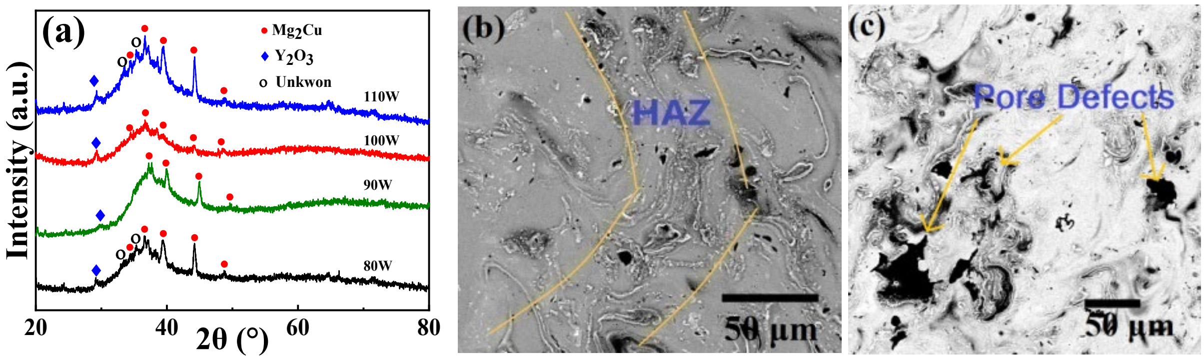

Figure 4. XRD and SEM of 3D-printed Mg-based metallic glasses with scanning speed of 1000 mm/s: (**a**) XRD of the samples with different laser power. (**b**) SEM of the cross-section with laser power of 110 W. (**c**) SEM of the cross-section with laser power of 80 W.

3.3. Mechanical Performance

Structural analysis shows that optimal laser power and scanning speed should be 100 W and 1000 mm/s, respectively. The Vickers hardness under such processing parameter is 249 ± 11. Figure 5a shows the compression test results of 3D-printed Mg-based metallic glasses under such processing parameters. The fracture strength is between 222 and 467 MPa, and no plastic strain is observed. The fracture strength is lower than that of the cast BMGs with the same composition. The variability of fracture strength was analyzed using the Weibull statistical method [20]. The double logarithmic form of the Weibull expression is

$$\ln\left\{\ln\left[\frac{1}{1-P_f}\right]\right\} = \ln V + m\ln\sigma - m\ln\sigma_0, \tag{1}$$

where P_f is the fracture probability, V is a normalized volume of the tested sample, m is the Weibull modulus, σ is the fracture strength, and σ_0 is a scaling parameter. The probability of failure, P_f, was calculated using the equation:

$$P_{f,i} = \frac{i-0.5}{\mathrm{n}}, \tag{2}$$

where n is the total number of tested samples, and i is the sample rank in ascending order of failure stress. Figure 5b shows the Weilbull plots suggested by Equation (1). Linear fitting of these data shows that the Weibull modulus m is 4.6 for 3D-printed Mg-based metallic glasses.

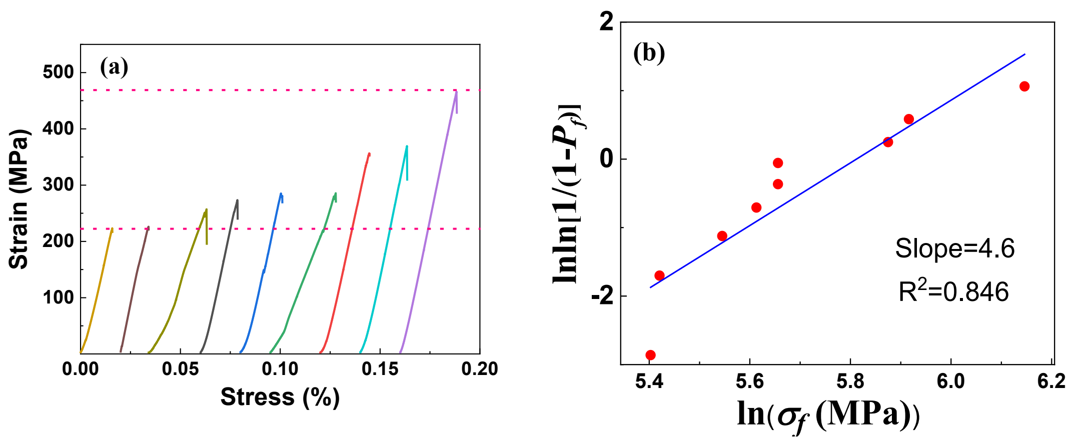

Figure 5. Compressive test results of 3D-printed Mg-based metallic glasses: (**a**) Compressive stress–strain curves from 9 samples. (**b**) Weibull plots of compressive fracture strength.

4. Discussion

4.1. Effects of Laser Energy Density on the Structures

The processing parameters and sample conditions are listed in Table 1. All the samples in the table are fabricated with a fixed layer thickness of 50 μm and a hatch spacing of 60 μm. Both laser power and scanning speed have an influence on the structure of 3D-printed Mg-based metallic glasses. The laser energy density parameter contains both laser power and scanning speed, and it is a popular parameter to optimize the microstructures of conventional crystalline alloys as well as BMGs produced by 3D printing [21]. It is defined as $U = P/(vth)$, where P is the laser power, v is the scanning speed, t is the hatch spacing, and h is the layer thickness. In our study, the hatch spacing is fixed at 60 μm, and the layer thickness is fixed at 50 μm. The optimal laser power and scanning speed are 100 W and 1000 mm/s, respectively, and they correspond to a laser energy density of 33.3 J/mm^2. It has been reported that the increment of laser energy density causes crystallization in HAZ, while the decrement of laser energy density causes pore defects [21,22]. The laser energy density is 37.0 J/mm^2 for a laser power of 100 W and a scanning speed of 900 mm/s, and it is 36.7 J/mm^2 for a laser power of 110 W and a scanning speed of 1000 mm/s. Under such parameters, the XRD curves show sharp crystalline peaks, and SEM images show thick HAZs, both indicating more crystalline phases. As the input of energy increases, the long duration at a high temperature in HAZ facilitates the growth of crystalline phases. The laser energy density is 40.7 J/mm^2 for a laser power of 110 W and a scanning speed of 900 mm/s. Under such high laser energy density, the samples show macrocracks. The increment of laser energy causes severe crystallization, and the brittle crystalline phases cannot inhibit the propagation of cracks caused by thermal stresses. The laser energy density is 27.7 J/mm^2 for a laser power of 100 W and a scanning speed of 1200 mm/s, and it is 26.7 J/mm^2 for a laser power of 80 W and a scanning speed of 1000 mm/s. Under such parameters, the SEM images show irregular pore defects with a size of tens of microns. It has been reported that the pore defects with such a size are considered to be caused by trapped gas in molten pools [23]. The XRD curves show sharp crystalline peaks under such laser energy densities. The pores are not good thermal conductors, and more heat is trapped inside the samples during fabrication, which profits the crystallization process. The laser energy density is 22.2 J/mm^2 for a laser power of 80 W and a scanning speed of 1200 mm/s. At such low energy density, the input energy does not melt the powder particles completely, so the samples do not show metallurgical combination. Our orthogonal experiment of laser power and scanning speed agrees with laser energy density very well. However, there are controversies regarding the reliability of laser energy density [24]. The laser energy density has four variables, and different combinations could give the same laser energy density. Detailed experiments are needed to clarify the effects of the four variables under the same laser energy density.

Table 1. Sample conditions with different processing parameters.

Energy Density (J/mm^2)	Laser Power (W)	Scanning Speed (mm/s)	Main Features
22.2	80	1200	Unfused powder
26.7	80	1000	Tens of microns irregular pores
27.7	100	1200	Tens of microns irregular pores
33.3	100	1000	23% crystallinity
36.7	110	1000	29% crystallinity
37.0	100	900	31% crystallinity
40.7	110	900	Macrocrack

4.2. Mechnical Performance

One of the enduring attractions of BMGs is their unique mechanical properties. However, 3D-printed BMGs experience different thermal histories, and the possible structural heterogeneities and defects may have a significant influence on the mechanical properties. It has been reported that 3D-printed tough Zr-based and Ti-based BMGs have similar fracture strength compared to their as-cast counterparts, but 3D-printed brittle BMGs such as Fe-based ones usually have much lower fracture strength than their as-cast counterparts [11,24,25]. The 3D-printed Mg-based metallic glasses show lower and more scattered fracture strength than that of the conventional cast ones. The fracture strength of the cast $Mg_{65}Cu_{20}Zn_5Y_{10}$ is 764–881 MPa, but the fracture strength of the 3D-printed ones is 222–467 MPa [18]. Both the 3D-printed and as-cast Mg-based metallic glasses do not show any plastic deformation in their compressive stress-strain curves. The Weibull modulus m of the 3D-printed Mg-based metallic glass is 4.6, close to brittle engineering ceramic materials. It has been reported that some cast Mg-based BMGs have Weibull moduli of 26 and 41 [20]. The smaller m value of the 3D-printed Mg-based metallic glasses denotes a wider distribution of fracture strength and lower reliability. The deteriorated mechanical performance of 3D-printed Mg-based metallic glasses is due to defects such as pores and precipitated crystalline phases [8]. While pore defects are hard to completely remove by optimization of the processing parameters, precipitated crystalline phases can be inhibited by the decrement of laser energy density. However, large pore defects appear if the laser energy density is too low. In our study, the precipitated crystalline phases are not completely inhibited until large pore defects appear. An effective approach to improve the mechanical properties of 3D-printed metallic glasses is to synthesize metallic glass matrix composites [26,27]. Some Mg-based metallic glass matrix composites are suitable for 3D printing, and our study provides a starting point for processing parameters [18,28,29].

5. Conclusions

Mg-based metallic glass can be fabricated by laser-based powder bed fusion (also known as selective laser melting) under a proper scanning speed and laser power. The 3D-printed Mg-based metallic glasses show lower and more scattered fracture strengths compared with their as-cast counterparts, and more efforts are needed to improve the mechanical performances. The main conclusions of this article are as follows:

1. The optimal energy density for 3D printing $Mg_{65}Cu_{20}Zn_5Y_{10}$ metallic glass is 33.3 J/mm^2, with a laser power of 100 W, a scanning speed of 1000 mm/s, a layer thickness of 50 μm, and a hatch spacing of 60 μm, respectively.
2. The decrement of laser energy density causes large pore defects, and further decreasing leads to unfused powder. The increment of laser energy density caused more crystalline phases in HAZs, and further increasing leads to macrocracks.
3. The 3D-printed Mg-based metallic glasses show deteriorated mechanical performances, and Weibull statistics show that they are less reliable than their as-cast counterparts.

Author Contributions: Conceptualization, K.Z.; methodology, Z.Z.; investigation, Z.Z., G.Y. and K.Z.; writing—original draft preparation, K.Z.; writing—review and editing, Z.Z. and G.Y. All authors have read and agreed to the published version of the manuscript.

Funding: This research was funded by Development Fund of Guiding Local Science and Technology by Central Government, grant number 206Z1806G, and Support Project for 100 Distinguished Scholars in Universities of Hebei Province, grant number SLRC2019050, and Hebei Province Three Scholar Program from Hebei Provincial Department of Human Resources and Social Security, grant number B20221004.

Data Availability Statement: Not applicable.

Conflicts of Interest: The authors declare no conflict of interest.

References

1. Hufnagel, T.C.; Schuh, C.A.; Falk, M.L. Deformation of Metallic Glasses: Recent Developments in Theory, Simulations, and Experiments. *Acta Mater.* **2016**, *109*, 375–393. [CrossRef]
2. Sun, B.A.; Wang, W.H. The Fracture of Bulk Metallic Glasses. *Prog. Mater. Sci.* **2015**, *74*, 211–307. [CrossRef]
3. Li, Y.C.; Zhang, C.; Xing, W.; Guo, S.F.; Liu, L. Design of Fe-Based Bulk Metallic Glasses with Improved Wear Resistance. *ACS Appl. Mater. Interfaces* **2018**, *10*, 43144–43155. [CrossRef] [PubMed]
4. Pang, S.J.; Zhang, T.; Asami, K.; Inoue, A. Synthesis of Fe–Cr–Mo–C–B–P Bulk Metallic Glasses with High Corrosion Resistance. *Acta. Mater.* **2002**, *50*, 489–497. [CrossRef]
5. Poomathi, N.; Singh, S.; Prakash, C.; Subramanian, A.; Sahay, R.; Cinappan, A.; Ramakrishna, S. 3D Printing in Tissue Engineering: A State of the Art Review of Technologies and Biomaterials. *Rap. Prot. J.* **2020**, *26*, 1313–1334. [CrossRef]
6. Khorasani, M.; Ghasemi, A.; Rolfe, B.; Gibson, I. Additive Manufacturing a Powerful Tool for the Aerospace Industry. *Rap. Prot. J.* **2022**, *28*, 87–199. [CrossRef]
7. Mehrpouya, M.; Tuma, D.; Vaneker, T.; Mohamadreza, A.; Afrasiabi, M.; Bambach, M.; Gibson, I. Multimaterial Power Bed Fusion Techniques. *Rap. Prot. J.* **2022**, *28*, 1–19. [CrossRef]
8. Zhang, C.; Ouyang, D.; Pauly, S.; Liu, L. 3D printing of Bulk Metallic Glasses. *Mater. Sci. Eng. R* **2021**, *145*, 100625. [CrossRef]
9. Li, X.P.; Roberts, M.P.; O'Keeffe, S.; Sercombe, T.B. Selective Laser Melting of Zr-based Bulk Metallic Glasses: Processing, Microstructure and Mechanical Properties. *Mater. Des.* **2016**, *112*, 217–226. [CrossRef]
10. Wang, L.; Wang, H.; Liu, Y.; Fu, Z.; Peng, T.; Shen, J.; Zhou, S.; Yan, M.; Wang, G.; Dai, Y. Selective Laser Melting Helps Fabricate Record-large Bulk Metallic Glass: Experiments, Simulation and Demonstrative Part. *J. Alloy. Comp.* **2019**, *808*, 151731. [CrossRef]
11. Deng, L.; Wang, S.; Wang, P.; Kuhn, U.; Pauly, S. Selective Laser Melting of a Ti-based Bulk Metallic Glass. *Mater. Lett.* **2018**, *212*, 346–349. [CrossRef]
12. Deng, L.; Zhang, L.; Kosiba, K.; Limbach, R.; Wondraczek, L.; Wang, G.; Gu, D.D.; Kuhn, U.; Pauly, S. CuZr-based Bulk Metallic Glass and Glass Matrix Composites Fabricated by Selective Laser Melting. *J. Mater. Sci. Tech.* **2021**, *81*, 139–150. [CrossRef]
13. Madge, S.V.; Greer, A.L. Laser Additive Manufacturing of Metallic Glasses; Issues in Vitrification and Mechanical Properties. *Oxf. Open Mater. Sci.* **2021**, *1*, 1–13. [CrossRef]
14. Zberg, B.; Uggowitzer, P.J.; Loffler, J.F. MgZnCa Glasses without Clinically Observable Hydrogen Evolution for Biodegradable Implants. *Nat. Mater.* **2009**, *8*, 887–891. [CrossRef]
15. Bin, S.J.B.; Fong, K.S.; Chua, B.W.; Gupta, M. Mg-based Bulk Metallic Glasses: A Review of Recent Development. *J. Magnes. Alloy.* **2022**, *10*, 899–914. [CrossRef]
16. Jin, C.; Liu, Z.; Yu, W.; Qin, C.; Yu, H.; Wang, Z. Biodegradable Mg-Zn-Ca-Based Metallic Glasses. *Materials* **2022**, *15*, 2172. [CrossRef] [PubMed]
17. Men, H.; Hu, Z.Q.; Xu, J. Bulk Metallic Glass Formation in the Mg-Cu-Zn-Y System. *Scr. Mater.* **2002**, *46*, 699–703. [CrossRef]
18. Hui, X.; Wei, D.; Wang, M.; Liu, X.; Yu, J.; Chen, G. In-situ $Mg_{77}Cu_{12}Zn_5Y_6$ Bulk Metallic Glass Matrix Composite with Extraordinary Plasticity. *Chin. Sci. Bull.* **2006**, *51*, 229–234. [CrossRef]
19. Pacheco, V.; Karlsson, D.; Marattukalam, J.J.; Stolpe, M.; Hjorvarsson, B.; Jansson, U.; Sahlberg, M. Thermal Stability and Crystallization of a Zr-based Metallic Glass Produced by Suction Casting and Selective Laser Melting. *J. Alloys Comp.* **2020**, *825*, 153995. [CrossRef]
20. Zhao, Y.Y.; Ma, E.; Xu, J. Reliability of Compressive Fracture Strength of Mg-Zn-Ca Bulk Metallic Glasses: Flaw Sensitivity and Weibull Statistics. *Scr. Mater.* **2008**, *58*, 496–499. [CrossRef]
21. Ouyang, D.; Xing, W.; Li, N.; Li, Y.; Liu, L. Structural Evolutions in 3D-printed Fe-based Metallic Glass Fabricated by Selective Laser Melting. *Addit. Manuf.* **2018**, *23*, 246–252. [CrossRef]
22. Xing, W.; Ouyang, D.; Chen, Z.; Liu, L. Effect of Energy Density on Defect Evolution in 3D Printed Zr-based Metallic Glasses by Selective Laser Melting. *Sci. China Phys. Mech. Astron.* **2020**, *63*, 226111. [CrossRef]
23. Xiao, R.; Zhang, X. Problems and Issues in Laser Beam Welding of Aluminum-lithium Alloys. *J. Manuf. Proc.* **2014**, *16*, 166–175. [CrossRef]
24. Prashanth, K.G.; Scudino, S.S.; Maity, T.; Das, J.; Eckert, J. Is the Energy Density a Reliable Parameter for Materials Synthesis by Selective Laser Melting? *Mater. Res. Lett.* **2017**, *5*, 386–390. [CrossRef]
25. Zhang, C.; Li, X.M.; Liu, S.Q.; Liu, H.; Yu, L.J.; Liu, L. 3D Printing of Zr-based Bulk Metallic Glasses and Components for Potential Biomedical Applications. *J. Alloy. Comp.* **2019**, *790*, 963–973. [CrossRef]
26. Li, N.; Zhang, J.; Xing, W.; Ouyang, D.; Liu, L. 3D Printing of Fe-based Bulk Metallic Glass Composites with Combined High Strength and Fracture Toughness. *Mater. Des.* **2018**, *143*, 285–296. [CrossRef]
27. Gao, X.; Lin, X.; Yu, J.; Li, Y.; Hu, Y.; Fan, W.; Shi, S.; Huang, W. Selective Laser Melting(SLM) of In-situ Beta Phase Reinforced Ti/Zr-based Bulk Metallic Glass Matrix Composite. *Scr. Mater.* **2019**, *171*, 21–25. [CrossRef]
28. Qiu, K.Q.; Hu, N.N.; Zhang, H.B.; Jiang, W.H.; Ren, Y.L.; Liaw, P.K. Mechanical Properties and Fracture Mechanism of as-cast $Mg_{77}TM_{12}Zn_5Y_6$ (TM=Cu, Ni) Bulk Amorphous Matrix Composites. *J. Alloy. Comp.* **2009**, *478*, 419–422. [CrossRef]
29. Lee, J.I.; Ryu, W.H.; Yoon, K.N.; Park, E.S. In-situ synthesis of Mg-based Bulk Metallic Glass Matrix Composites with Primary α–Mg Phases. *J. Alloy. Comp.* **2021**, *879*, 160417. [CrossRef]